

Empirical Dust Models: Taking Hydrodynamical Simulations with a Grain of Dust

CHANGHOON HAHN^{1, 2, *} AND IQ COLLABORATORY

¹*Lawrence Berkeley National Laboratory, 1 Cyclotron Rd, Berkeley CA 94720, USA*

²*Berkeley Center for Cosmological Physics, University of California, Berkeley CA 94720, USA*

(Dated: DRAFT --- bbb80bf --- 2020-07-14 --- NOT READY FOR DISTRIBUTION)

ABSTRACT

We construct a dust empirical model (DEM) framework for applying dust attenuation to simulated galaxies based on handful of sensible assumptions that come from our understanding of dust attenuation. The DEM framework is essentially based on state-of-the-art attenuation curves with a flexible parameterization that allows us to statistically sample them. Applying DEMs to three different hydrodynamic simulations, SIMBA, Illustris TNG, and EAGLE, we are able to produce UV and optical photometry consistent with SDSS observations ($(G - R) - M_r$ color-magnitude and $(FUV - NUV) - M_r$ relations). This suggests that there's enough freedom in our current understanding (or lack) of dust for all simulations to reproduce observations. Meanwhile, the DEM provides some insights into dust as well as the subgrid physics that goes into the hydro simulations.

Keywords: keyword1 – keyword2 – keyword3

1. INTRODUCTION

dust is important because....

assumptions on the attenuation curve can dramatically impact the physical properties inferred from SED fitting (*e.g.* [Kriek & Conroy 2013](#); [?](#); [Reddy et al. 2015](#); [Salim & Narayanan 2020](#)).

motivation for an empirical dust attenuation model

attenuation vs extinction. While extinction curves have been derived from observations and theoretically, it's not easy to map this to attenuation curves. Attenuation curves are a product of complicated empirical processes since it accounts for light that gets scattered and star light that is not obscured

This makes modeling them in a complete physically motivated method expensive. People have done it [Narayanan et al. \(2018\)](#); [Trayford et al. \(2020\)](#). some detail about the radiative transfer method and such. But besides being expensive they have to make a number of assumptions anyway. *e.g.* [Narayanan et al. \(2018\)](#) assumes a fixed extinction curve.

* hahn.changhoon@gmail.com

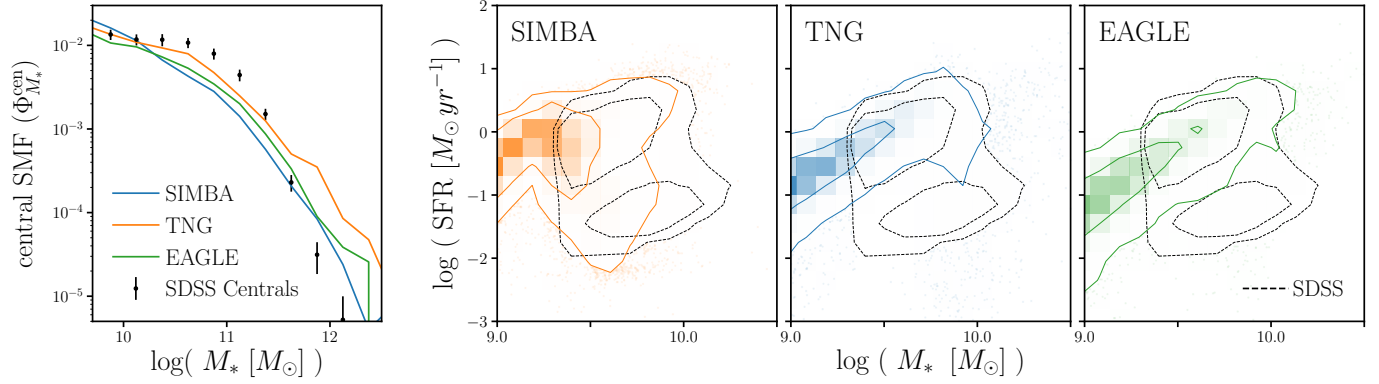


Figure 1. The stellar mass functions ($\Phi_{M_*}^{\text{cen}}$; left-most panel) and $M_* - \text{SFR}$ relation (right panels) of central galaxies from the SIMBA (orange), TNG (blue), and EAGLE (green) simulations. We include, for comparison, $\Phi_{M_*}^{\text{cen}}$ (black) and the $M_* - \text{SFR}$ relation (black dashed) for our SDSS central galaxy sample. Uncertainties for the SDSS $\Phi_{M_*}^{\text{cen}}$ are derived using jackknife resampling. In Section 2, we describe the simulations and observations above. Differences in $\Phi_{M_*}^{\text{cen}}$ and the $M_* - \text{SFR}$ relations among the simulations highlight how the *hydrodynamical simulations predict central galaxies with significantly different the physical properties*.

Moreover, because the radiative transfer method is expensive it's hard to compare many different simulations. Not only that, observables generated from simulations that take into radiative transfer dust models complicates simulation to simulation comparisons. Because you're simultaneously comparing the galaxy formation prescription and all the dust prescription.

emphasize somewhere here that using a prescription trained one sim doesn't translate well to other sims.

Instead, we present a framework using flexible dust empirical models that paints attenuation curves onto galaxies. describe at a high level how we are parameterizing DEMs

emphasize comparisons in observable space (Nelson et al. (2018) talks about importance of color)

talk about the advantages: extremely flexible so it can encompass the wide variety of attenuation curves found in radiative transfer, easy to correlate the attenuation curve with galaxy properties.

Also DEMs make it possible to statistically apply attenuation curves for large galaxy population. Putting this ontop of simulations, we can use them to generate observables and compare them to observations to constrain the DEM. This framework allows us to learn about attenuation curves given a model for galaxy formation.

Trayford et al. (2015) uses an empirical dust model but doesn't implement an attenuation curve but rather multiplicative factors for the broadband photometry.

The other way around also works. If you don't care about dust at all, DEM provides a framework to easily marginalize over dust attenuation and treat dust as a nuisance parameter.

In this paper, we do above for multiple simulations.

Starkenburger et al. in prep will use this framework to marginalize over dust and compare galaxy populations predicted by multiple simulations .

CH: why do we only do centrals?

2. DATA

In this paper we apply dust empirical models (DEM) to galaxies in the Illustris TNG, EAGLE, and SIMBA cosmological hydrodynamical simulations. We then measure the r -band luminosity (M_r), optical color ($G-R$), and UV color ($FUV-NUV$) of the DEM output from forward modeled spectral energy distributions (SED). These forward modeled observables, unlike physical properties such as M_* and SFR, are *consistently* defined and derived in both simulations and observations. Afterwards, we compare these predicted DEM observables to the central galaxies in SDSS DR7 observations. Below, we briefly describe the hydrodynamical simulations and the SDSS observations used throughout this work.

In Figure 1, we present the stellar mass functions ($\Phi_{M_*}^{\text{cen}}$; left-most panel) and $M_* - \text{SFR}$ relations (right panels) for central galaxies in the SIMBA (orange), TNG (blue), and EAGLE (green) simulations. We include, for reference, $\Phi_{M_*}^{\text{cen}}$ and the $M_* - \text{SFR}$ relation for our SDSS central galaxy sample. The uncertainties for the SDSS SMF are derived from jackknife resampling. For the simulations, M_* is the total stellar mass within the host halo, excluding any stellar mass in subhalos, and SFR is the instantaneous SFR derived from the rate of star formation in dense and cold gas. For SDSS, M_* is estimated using `kcorrect` (Blanton & Roweis 2007) assuming a Chabrier (2003) initial mass function and SFR are from the current release of Brinchmann et al. (2004)¹. We describe the simulations and observations further in sections below. Figure 1 illustrates that the hydrodynamical simulations have significantly different SMFs and $M_* - \text{SFR}$ relations. This difference, which was also recently highlighted in Hahn et al. (2019c), demonstrates that *the hydrodynamical simulations all predict central galaxy populations with significantly different physical properties*.

2.1. Illustris TNG

The Illustris TNG simulation² (hereafter TNG) is a cosmological hydrodynamical simulation of comoving volume (110.7 Mpc)³ (Nelson et al. 2018; Pillepich et al. 2018; Springel et al. 2018). It improves on the original Illustris simulation³ (Vogelsberger et al. 2014; Genel et al. 2014; public data release by Nelson et al. 2015), by including magneto-hydrodynamics and updated treatments for galactic winds, metal enrichment, and AGN feedback. Most notably, TNG uses a new implementation for feedback from SMBH (Weinberger et al. 2018), where feedback energy is injected in the form of a kinetic AGN-driven wind at low SMBH accretion rates. This new implementation has been shown to alleviate discrepancies found between the original Illustris and observations for $> 10^{13-14} M_\odot$ massive halos. **details on the following properties that we use in the paper: SFH, ZH**

TODO

2.2. EAGLE

We use L0100Ref of the Virgo Consortium’s EAGLE project⁴, a publicly available suite of cosmological hydrodynamic simulations (Schaye et al. 2015; Crain et al. 2015; McAlpine et al. 2016). The simulation has a comoving volume of (100 Mpc)³ and is simulated with the ANARCHY code (Dalla Vecchia et al. in prep.; see also Appendix A of Schaye et al. 2015), a modified version of the GADGET-3

¹ <http://www.mpa-garching.mpg.de/SDSS/DR7/>

² <https://www.tng-project.org/>

³ <http://www.illustris-project.org>

⁴ <http://www.eaglesim.org>

code (Springel 2005). It has subgrid models for star formation, stellar mass loss, metal enrichment and stellar feedback that stochastically inject thermal energy in the ISM as in (Dalla Vecchia & Schaye 2012); the feedback energy from AGN is also added to surrounding gas stochastically (Booth & Schaye 2009). Parameters of the stellar feedback and SMBH accretion are calibrated to broadly reproduce the $z = 0$ stellar mass function and galaxy stellar size-stellar mass relation. Meanwhile, the AGN feedback efficiency is calibrated to match the SMBH-galaxy mass relation. details on the following properties that we use in the paper: SFH, ZH TODO

2.3. SIMBA

The SIMBA simulation suite (Davé et al. 2019), the successor to MUFASA (Davé et al. 2016, 2017a,b), is a cosmological hydrodynamical simulation constructed using GIZMO, a meshless finite mass hydrodynamics code (Hopkins 2015; Hopkins et al. 2017). Of the simulations, we use ‘m100n1024’, which has a box size of $(100 h^{-1} \text{ Mpc})^3$ and baryonic mass resolution of $1.82 \times 10^7 M_\odot$. The simulation uses the same subgrid models as MUFASA for H_2 based star formation, decoupled two-phase winds for star formation driven galactic winds, and feedback from Type I supernovae and AGB stars. Meanwhile, it uses updated models for AGN feedback and on-the-fly dust model. SIMBA uses a two-mode SMBH accretion model, torque-limited accretion for cold gas (Anglés-Alcázar et al. 2017) and Bondi-based accretion for hot gas, and two-mode AGN feedback. details on the following properties that we use in the paper: SFH, ZH TODO

2.4. Forward Modeled Spectral Energy Distributions

describe how the SED is generated using the SFH and ZHs TODO

In Figure 2 we present the optical and UV color-magnitude relations, $(G-R) - M_r$ (top) and $(FUV-NUV) - M_r$ (bottom), for central galaxies of the SIMBA (left), TNG (center) and EAGLE (right) simulations. The $G-R$ and $FUV-NUV$ colors are derived from the forward modeled SED and absolute magnitudes. The observables for the simulations do not include any prescription for dust attenuation. Comparison to the observables of SDSS centrals (black dashed) clearly demonstrate that *without any dust attenuation, the hydrodynamical simulations cannot reproduce the observed optical or UV color-magnitude relations.*

2.5. SDSS DR7 Central Galaxies

The goal of the DEM we present in this paper is to provide a flexible model that can reproduce observations using the hydrodynamical simulations above. Throughout this work, we use the Tinker et al. (2011) SDSS central galaxy sample as our observation. This sample is constructed by first selecting a volume-limited sample of galaxies at $z \approx 0.04$ with $M_r < -18$ and complete above $M_* > 10^{9.4} h^{-2} M_\odot$ from the SDSS DR7 (Abazajian et al. 2009) NYU Value-Added Galaxy Catalog (VAGC; Blanton et al. 2005). Then, central galaxies are identified using a halo-based group finder that uses the abundance matching ansatz to iteratively assign halo masses to groups. Every group contains one central galaxy, which by definition is the most massive, and a group can contain ≥ 0 satellites. As with any group finder, galaxies are misassigned due to projection effects and redshift space distortions; however, the central galaxy sample has a purity of $\sim 90\%$ and completeness of $\sim 95\%$ (Tinker et al.

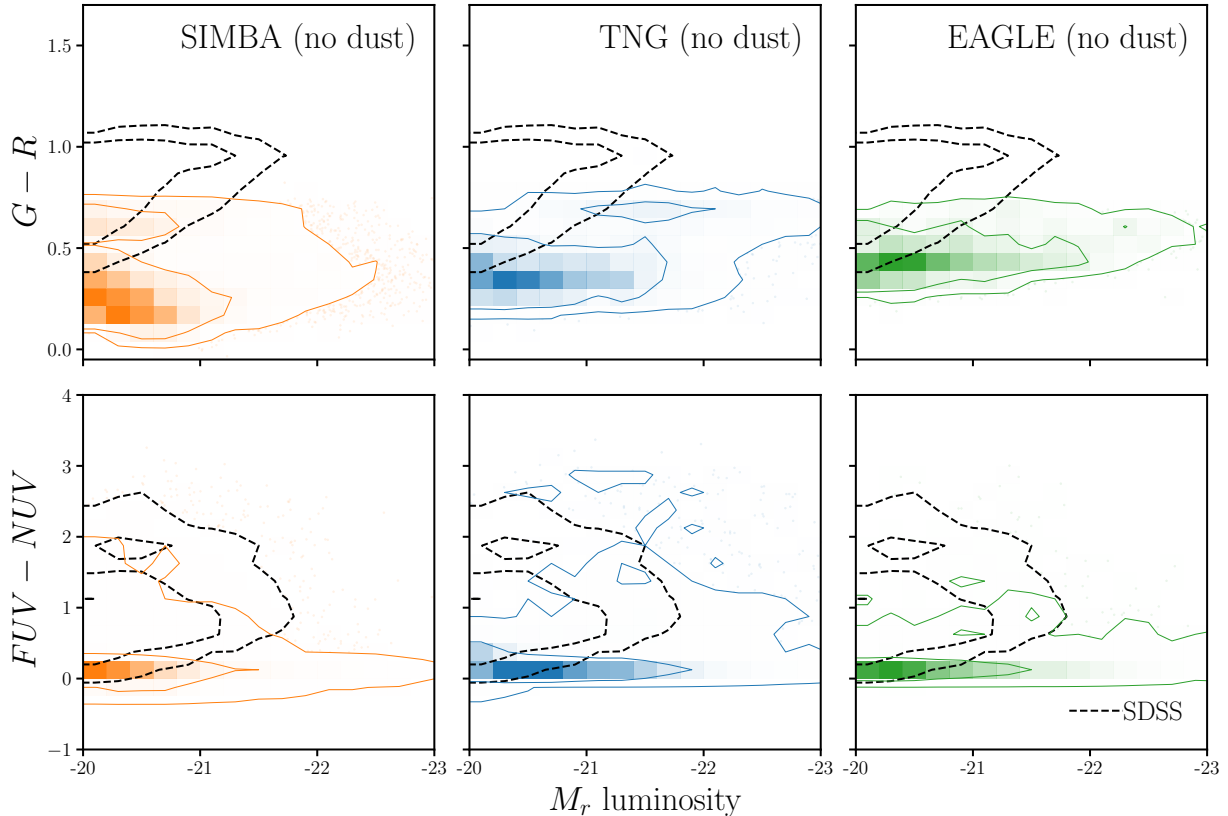


Figure 2. We present the optical and UV color-magnitude relations of central galaxies in the SIMBA (left), TNG (center), and EAGLE (right) simulations. The simulations above do *not* yet include the DEM or any prescription for dust attenuation. $(G-R) - M_r$ (top) and $(FUV-NUV) - M_r$ (bottom) are the main observables used throughout the paper. They are derived from forward modeled SEDs and, thus, are consistently defined and measured as SDSS observations (Section 2.4). For comparison, we include the distributions of SDSS centrals (black dashed). *Without dust, the hydrodynamical simulations cannot reproduce the observed optical or UV color-magnitude.*

2018). Finally, we impose a r -band absolute magnitude cut of $M_r < -20$ where our SDSS central galaxy sample is complete. In this work, we focus on observables that can be consistently defined and derived in both simulations and observables: M_r , $G-R$, and $FUV-NUV$. For our SDSS sample, we use r and g band absolute magnitudes from VAGC and GALEX FUV and NUV from the NASA-Sloan Atlas⁵.

3. DUST EMPIRICAL MODELING

In this section we present the dust empirical model (DEM), a flexible model for applying attenuation curves to galaxy populations that allows us to incorporate intrinsic variations in dust attenuation as well as correlation to physical galaxy properties. Later, we demonstrate that we can accurately

⁵ <http://nsatlas.org/>

reproduce observations with the DEM and use it to test galaxy formation models and shed light on dust in galaxies.

We define the dust attenuation curve $A(\lambda)$ as

$$F_o(\lambda) = F_i(\lambda)10^{-0.4A(\lambda)} \quad (1)$$

where F_o is the observed flux and F_i is the intrinsic flux. We normalize the attenuation at the V band,

$$A(\lambda) = A_V \frac{k(\lambda)}{k_V} \quad (2)$$

so that A_V determines the amplitude of the attenuation, while $k(\lambda)$ determines the wavelength dependence.

To determine $A(\lambda)$ for each galaxy, we first assign A_V using the slab model from [Somerville & Primack \(1999\)](#); [Somerville et al. \(2012\)](#). In the slab model, A_V is calculated from the inclination of the galaxy, i , and its optical depth, τ_V :

$$A_V = -2.5 \log \left[\frac{1 - e^{-\tau_V \sec i}}{\tau_V \sec i} \right]. \quad (3)$$

For all of our galaxies, we uniformly sample i . Then, we include the correlation between A_V and galaxy properties (M_* and SFR), found in both observations and simulations (*e.g.* [Narayanan et al. 2018](#); [Salim & Narayanan 2020](#)), in τ_V . We use τ_V with a simple and flexible linear M_* and SFR dependence:

$$\tau_V(M_*, \text{SFR}) = m_{\tau, M_*} \log \left(\frac{M_*}{10^{10} M_\odot} \right) + m_{\tau, \text{SFR}} \log \text{SFR} + c_\tau. \quad (4)$$

m_{τ, M_*} quantifies the M_* dependence, $m_{\tau, \text{SFR}}$ quantifies the SFR dependence, and c_τ quantifies the overall amplitude. Since τ_V is optical depth, we impose a $\tau_V \geq 0$ limit. We note that the slab model is a naive approximation. In reality, A_V for a galaxy will depend on complexities of its star-to-dust geometry, variations in the extinction curves, and other properties beyond just inclination and τ_V . The purpose of the DEM, however, is not to accurately model dust attenuation for individual galaxies, but rather to accurately model the distribution of dust attenuation of galaxy populations. In this sense, the slab model qualitatively reproduces the correlation between A_V and i found in the literature: edge-on galaxies have higher A_V than face-on galaxies (*e.g.* [Salim & Narayanan 2020](#)). More importantly, the distribution of A_V , $p(A_V)$, produced using the slab model with uniformly sampled inclinations closely matches the $p(A_V)$ of our SDSS sample (Figure 8). Also, we demonstrate that replacing the slab model with a more flexible prescription for sampling A_V does not significantly impact our analysis (Appendix B). We therefore conclude that the slab model is a sufficiently flexible empirical prescription for sampling A_V .

For the wavelength dependence of the attenuation curve, $k(\lambda)$, we use the [Noll et al. \(2009\)](#) parameterization:

$$k(\lambda) = (k_{\text{Cal}}(\lambda) + D(\lambda)) \left(\frac{\lambda}{\lambda_V} \right)^\delta. \quad (5)$$

Here $k_{\text{Cal}}(\lambda)$ is the Calzetti (2001) curve:

$$k_{\text{Cal}}(\lambda) = \begin{cases} 2.659(-1.857 + 1.040/\lambda) + R_V, & 6300\text{\AA} \leq \lambda \leq 22000\text{\AA} \\ 2.659(-2.156 + 1.509/\lambda - 0.198/\lambda^2 + 0.011/\lambda^3) + R_V & 1200\text{\AA} \leq \lambda \leq 6300\text{\AA} \end{cases}$$

where $\lambda_V = 5500\text{\AA}$ is the V band wavelength. δ is the slope offset of the attenuation curve from k_{Cal} . Since δ correlates with galaxy properties (*e.g.* Leja et al. 2017; Salim et al. 2018), we parameterize δ with a similar M_* and SFR dependence as τ_V :

$$\delta(M_*, \text{SFR}) = m_{\delta, M_*} \log \left(\frac{M_*}{10^{10} M_\odot} \right) + m_{\delta, \text{SFR}} \log \text{SFR} + c_\delta \quad (6)$$

$D(\lambda)$ in Eq. 5 is the UV dust bump, which we parameter using the standard Lorentzian-like Drude profile:

$$D(\lambda) = \frac{E_b(\lambda\Delta\lambda)^2}{(\lambda^2 - \lambda_0^2)^2 + (\lambda\Delta\lambda)^2} \quad (7)$$

where λ_0 , $\Delta\lambda$, and E_b are the central wavelength, FWHM, and strength of the bump, respectively. We assume fixed $\lambda_0 = 2175\text{\AA}$ and $\Delta\lambda = 350\text{\AA}$. Kriek & Conroy (2013) and Tress et al. (2018) find that E_b correlates with the δ for star-forming galaxies $z \sim 2$. Narayanan et al. (2018) confirmed this dependence in simulations. In our DEM, we assume a fixed relation between E_b and δ from Kriek & Conroy (2013): $E_b = -1.9 \delta + 0.85$. We note that allowing the slope and amplitude of the E_b and δ relation to vary, does *not* impact our results.

Next, to attenuate the galaxy SEDs, we apply $A(\lambda)$ we separately to the star light and nebular emission:

$$F_o(\lambda) = F_i^{\text{star}}(\lambda)10^{-0.4A(\lambda)} + F_i^{\text{neb}}(\lambda)10^{-0.4A_{\text{neb}}(\lambda)}. \quad (8)$$

We parameterize

$$A_{\text{neb}}(\lambda) = f_{\text{neb}}A(\lambda) \quad (9)$$

and allow f_{neb} to vary freely. In Table 1, we list and describe all of the free parameters in the DEM.

SFR of galaxies are used to calculate τ_v and δ in Eqs. 4 and 6. Due to mass and temporal resolutions, some galaxies in the simulations have $\text{SFR} = 0$ — *i.e.* an unmeasurably low SFR (Hahn et al. 2019c). Eqs. 4 and 6 cannot be used to derive τ_v and δ for these galaxies. Since $\text{SFR} = 0$ galaxies do not account for a large fraction of our simulated galaxies, we directly sample their observables (G , R , NUV , and FUV) from the distribution of observables for SDSS quiescent galaxies. This way, the attenuation of $\text{SFR} = 0$ galaxies does not impact the rest of the DEM parameters. In Appendix A, we discuss the resolution effects in more detail and demonstrate that our results are *not* impacted by other prescriptions for attenuating $\text{SFR} = 0$ galaxies.

In practice, for a simulated galaxy population, we first uniformly sample inclinations, i , and assign them to each galaxy. Then for a given set of DEM parameter values (Table 1), τ_V , and δ are calculated for each galaxy using its i , M_* , and SFR. From τ_v and δ , we get A_V and $k(\lambda)$, which together gives $A(\lambda)$ for all the galaxies. Afterwards, we attenuate the galaxy SEDs using Eq. 8 and use the attenuated SEDs to calculate our observables: the G , R , NUV , and FUV absolute magnitudes.

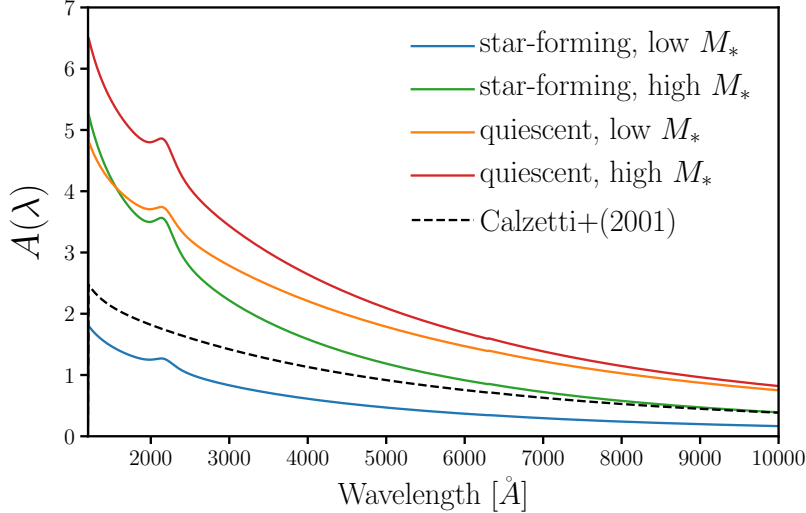


Figure 3. Attenuation curves, $A(\lambda)$, of our Dust Empirical Model (DEM) for galaxies with different SFR and M_* . We include $A(\lambda)$ for star-forming (SFR = $10^{0.5} M_\odot/\text{yr}$) low mass galaxy ($10^{10} M_\odot$; blue), high mass galaxy ($10^{11} M_\odot$; green) and quiescent (SFR = $10^{-2} M_\odot/\text{yr}$) low mass galaxy ($10^{10} M_\odot$; orange), high mass galaxy ($10^{11} M_\odot$; red). All galaxies are edge-on (*i.e.* $i = 0$) and we use arbitrary DEM parameter values $\{m_{\tau, M_*}, m_{\tau, \text{SFR}}, c_\tau, m_{\delta, M_*}, m_{\delta, \text{SFR}}, c_\delta\} = \{2., -2., 2., -0.1, -0.1, -0.2\}$ within the prior range (Table 1). For comparison, we include the Calzetti (2001) attenuation curve. In the DEM, the amplitude, slope, and UV dust bump of $A(\lambda)$ depend on M_* , and SFR (Eqs. 4 and 6). *The DEM provides a flexible model for assigning dust attenuation to galaxies based on their physical properties.*

In Figure 3, we present the DEM $A(\lambda)$ for galaxies with different SFR and M_* : star-forming (SFR = $10^{0.5} M_\odot/\text{yr}$) with low mass ($10^{10} M_\odot$; blue), with high mass ($10^{11} M_\odot$; green) and quiescent (SFR = $10^{-2} M_\odot/\text{yr}$) with low mass ($10^{10} M_\odot$; orange), with high mass ($10^{11} M_\odot$; red). All galaxies are edge-on (*i.e.* $i = 0$) and we use $\{m_{\tau, M_*}, m_{\tau, \text{SFR}}, c_\tau, m_{\delta, M_*}, m_{\delta, \text{SFR}}, c_\delta\} = \{2., -2., 2., -0.1, -0.1, -0.2\}$, which were arbitrarily chosen within the prior range listed in Table 1. For comparison, we include the Calzetti (2001) attenuation curve. The DEM we describe in this section provides a flexible model for assigning dust attenuation to galaxies based on their physical properties.

4. SIMULATION-BASED INFERENCE: APPROXIMATE BAYESIAN COMPUTATION

The DEM provides a flexible model to apply dust attenuation to central galaxies from the hydrodynamic simulations (Section 2) and derive observables which can be directly compared to SDSS observations. For the comparison and the inference of DEM parameters, we use Approximate Bayesian Computation (hereafter ABC; Diggle & Gratton 1984; Tavaré et al. 1997; Pritchard et al. 1999; Beaumont et al. 2009; Del Moral et al. 2012). ABC is a simulation-based (or “likelihood-free”) parameter inference framework that approximates the posterior probability distribution, $p(\theta | \text{data})$, without requiring evaluations of the likelihood. Instead, ABC only requires a forward model of the observed data, a prior that can be sampled, and a distance metric that quantifies the “closeness” to the observed data. Since ABC does not require evaluating the likelihood, it does not assume any functional form of the likelihood, which can significantly bias the inferred posterior Hahn et al. (2019b). It also

Table 1. Parameters of the Dust Empirical Model

Parameter	Definition	prior
m_{τ,M_*}	Slope of the optical depth, τ_V , $\log M_*$ dependence	flat $[-5., 5.]$
$m_{\tau,\text{SFR}}$	Slope of the optical depth, τ_V , $\log \text{SFR}$ dependence	flat $[-5., 5.]$
c_τ	amplitude of the optical depth, τ_V	flat $[0., 6.]$
m_{δ,M_*}	Slope of the attenuation curve slope offset, δ , $\log M_*$ dependence	flat $[-4., 4.]$
$m_{\delta,\text{SFR}}$	Slope of the attenuation curve slope offset, δ , $\log \text{SFR}$ dependence of	flat $[-4., 4.]$
c_δ	amplitude of the attenuation curve slope offset, δ	flat $[-4., 4.]$
f_{neb}	nebular attenuation fraction	flat $[1., 4.]$

enables us to estimate the posterior using observables with difficult or intractable likelihoods [Hahn et al. \(2017a\)](#).

In the simplest version of ABC with a rejection sample framework ([Pritchard et al. 1999](#)), a proposal set of parameter values are drawn from the prior. The forward model is run with the proposal parameter values. Then the output of the forward model is then compared to the observed data using the distance metric and a distance threshold. Proposals are drawn until enough of them pass the threshold to sample the posterior. A rejection sampling framework requires a large number of evaluations of the forward model, which can be computationally costly. Many variations of ABC with more efficient sampling strategies have now been applied to astronomy and cosmology (*e.g.* [Cameron & Pettitt 2012](#); [Weyant et al. 2013](#); [Ishida et al. 2015](#); [Lin et al. 2016](#); [Alsing et al. 2018](#)). Among these methods, we use ABC in conjunction with Population Monte Carlo (PMC) importance sampling ([Hahn et al. 2017a,b, 2019a](#)).

The forward model in our scenario is the hydrodynamic simulation combined with the DEM. Given a set of values for the DEM parameters, our forward model produces G , R , NUV , and FUV absolute magnitudes, which can be directly compared to SDSS observations. We use uninformative uniform priors on each of the DEM parameters and choose ranges to encompass constraints in the literature. The prior ranges of m_{τ,M_*} , $m_{\tau,\text{SFR}}$, c_τ are chosen to conservatively include the A_V range and M_* and SFR dependence of [Narayanan et al. \(2018\)](#) and [Salim & Narayanan \(2020\)](#). Meanwhile, the prior ranges of m_{δ,M_*} , $m_{\delta,\text{SFR}}$, c_δ are chosen to conservatively include the δ range and M_* and SFR dependence of [Leja et al. \(2017\)](#) and [Salim et al. \(2018\)](#). We list the range of the priors in Table 1. We note that uniform priors on the DEM parameters do not result in uniform priors on τ_V or δ (*e.g.* [Handley & Millea 2019](#)). However, we are interested in marginalizing over dust attenuation and understanding the dependence of dust attenuation on galaxy properties, so we use uninformative priors on the DEM parameters and not on the derived τ_V or δ .

ABC also requires a distance metric that quantifies the “closeness” of the forward model output to the observed data. For our distance metric, we use the L2 norm between the summary statistics of the SDSS observation and our forward model:

$$\bar{\rho}(\theta_{\text{DEM}}) = [X^{\text{SDSS}} - X^{\text{FM}}(\theta_{\text{DEM}})]^2. \quad (10)$$

θ_{DEM} are the DEM parameters. The summary statistics are based on the optical and UV color-magnitude, $(G-R)-R$ and $(FUV-NUV)-R$, relations of central galaxies brighter than $M_r < -20$, where our SDSS central galaxy sample is complete (Figure 2). More specifically, for X , we calculate the number density in 3D bins of $G-R$, $FUV-NUV$, and M_r with widths 0.0625, 0.25, and 0.5 mags. We choose this summary statistic to fully exploit the observable-space predicted by the forward model. Later in Section 5 we discuss other observables that could be included in the analysis.

ABC-PMC begins by first with an arbitrarily large threshold ϵ_1 and N proposals $\bar{\theta}_1$ sampled from the prior distribution. Each proposal is assigned a weight $w_1^i = 1/N$. Then for subsequent iterations ($i > 1$), the threshold, ϵ_i , is set to the median distance of the previous iteration’s proposals. New proposals are drawn from the previous iteration’s proposals perturbed by a kernel and kept if their distance is below ϵ_i . This is repeated until we assemble a new set of N proposals $\bar{\theta}_i$. The entire process is repeated for the next iteration until convergence is confirmed. For further details on the ABC-PMC implementation, we refer readers to Hahn et al. (2017b) and Hahn et al. (2019a). In Figure 4, we present the posterior distributions of the DEM parameters derived from ABC-PMC for the SIMBA (orange), TNG (blue), and EAGLE (green) hydrodynamical simulations. The contours mark the 68% and 95% confidence intervals.

5. RESULTS

In Figure 5, we present the optical and UV color-magnitude relations predicted by the DEM with the median ABC posteriors for the SIMBA (orange), TNG (blue), and EAGLE (green) simulations. We include the SDSS observables for comparison (black dashed). Without any dust attenuation, we previously found that simulations predict dramatically different $(G-R)-M_r$ and $(FUV-NUV)-M_r$ relations than SDSS (Figure 2). In contrast, with the DEM, the optical color-magnitude relations have well-defined red sequences and blue clouds that are consistent with SDSS. The DEM also produces galaxies with $FUV-NUV$ distributions that are consistent with SDSS. We also find good agreement in the galaxy number density at $M_r < -20$: **CH: numbers**

Previous works in the literature have also compared colors and luminosities predicted by simulations to observations. For EAGLE, Trayford et al. (2015) calculate colors and luminosities with the GALAXEV population synthesis models and a two-component screen model for dust. More recently, Trayford et al. (2017) calculated optical colors for EAGLE using SKIRT, a Monte Carlo radiative transfer code (Camps & Baes 2015), to model the dust. Both Trayford et al. (2015) and Trayford et al. (2017) produce bluer red sequences compared to GAMA observations, at $10^{11.2} < M_* < 10^{11.5}$ for Trayford et al. (2017). Although a detailed comparison is difficult since both works examine all galaxies, not only centrals, the DEM accurately reproduces the position of the SDSS red sequence, even at high M_* . Trayford et al. (2015) also predict significant more luminous blue galaxies than observations or the DEM. Using the same Trayford et al. (2017) SKIRT framework, Baes et al. (2019) find that they overestimate the observed cosmic spectral energy distributions (CSED) in the UV regime. Moreover, the $FUV-NUV$ color of their CSED is significantly higher than GAMA $FUV-NUV$. The DEM, on the other hand, predict $FUV-NUV$ in good agreement with SDSS. For TNG, Nelson et al. (2018) calculate optical colors using a dust model that includes attenuation due to dense gas birth clouds surrounding young stellar populations and also due to simulated distribution of neutral

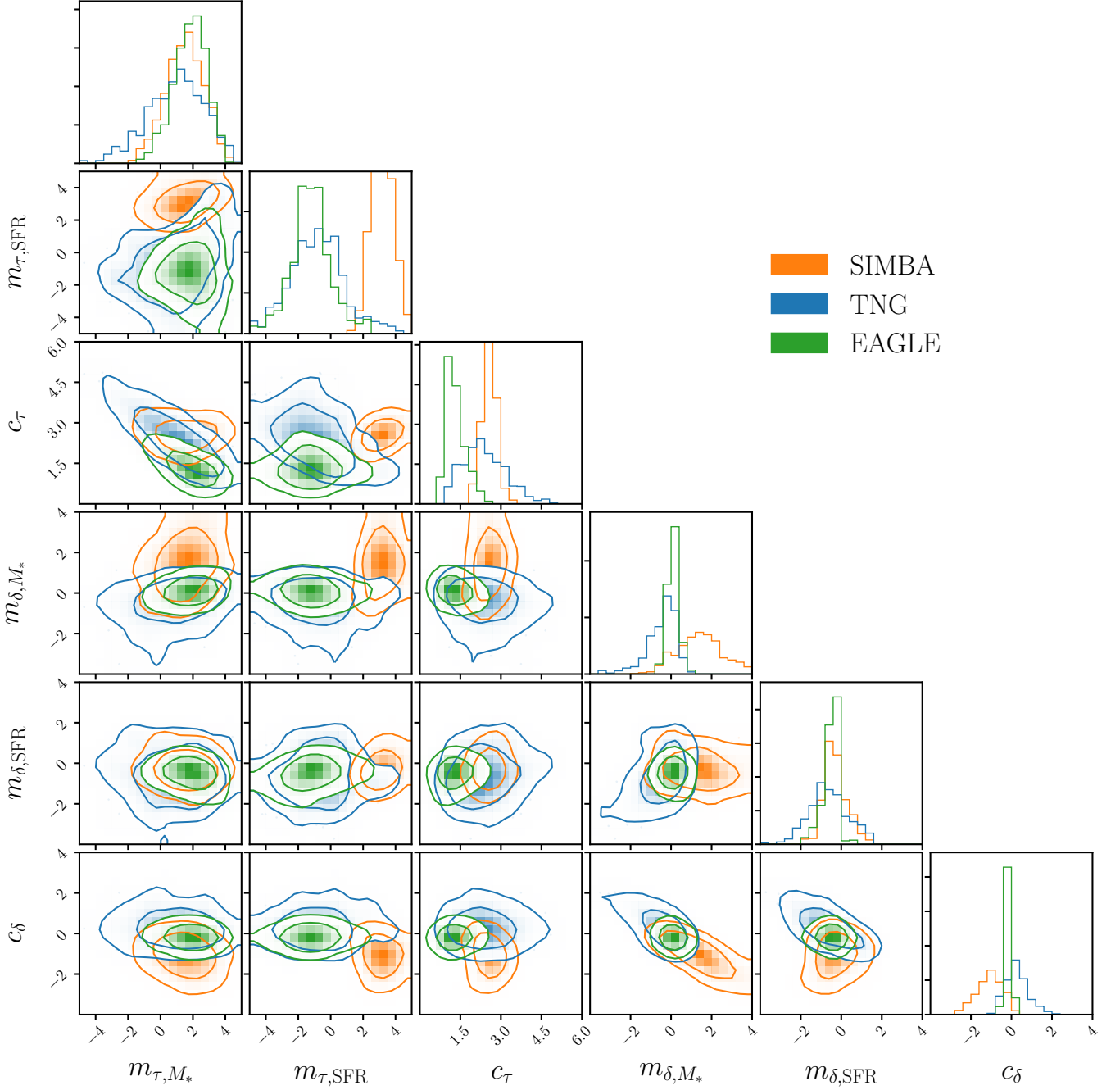


Figure 4. Posterior distributions of DEM parameters for the SIMBA (orange), TNG (blue), and EAGLE (green) hydro simulations. The contours mark the 68% and 95% confidence intervals. The posteriors are derived using Approximate Bayesian Computation with Population Monte Carlo (Section 4). **CH: REVISIT:** In all simulations, dust attenuation increases for higher M_* galaxies ($m_{\tau, M_*} \sim 2$). The simulations also have consistent optical depth amplitudes (c_{τ}). However, the SFR dependence of τ_V is different among the simulations. For TNG and EAGLE, star-forming galaxies have lower τ_V ; for SIMBA quiescent galaxies have lower τ_V . Meanwhile, for the slope offset of the attenuation curve, δ , we find little M_* and SFR dependence in the simulations and that the amplitude (c_{τ}) is consistent with 0.

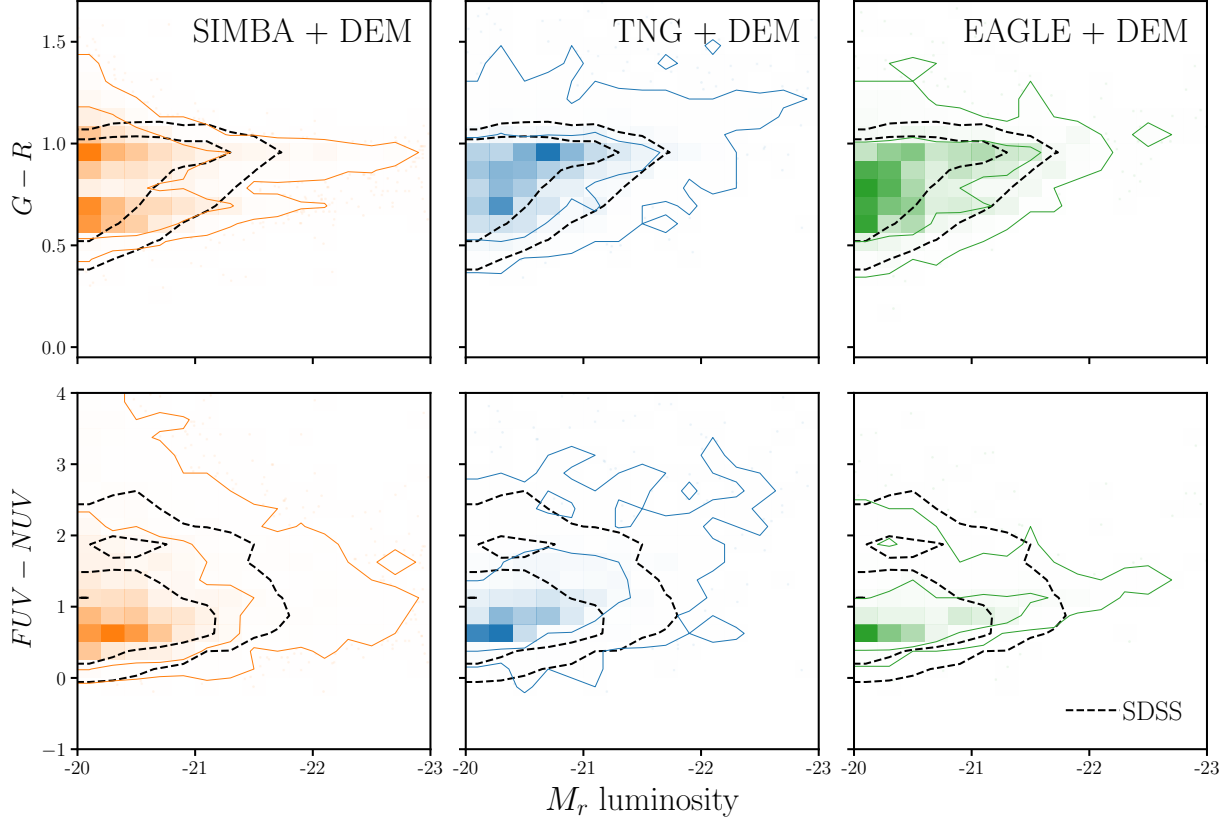


Figure 5. The optical and UV color-magnitude relations predicted by the DEM with the median ABC posteriors for the SIMBA (orange), TNG (blue), and EAGLE (green) hydrodynamical simulations. For comparison, we include the $(G-R) - M_r$ (top panels) and $(FUV-NUV) - M_r$ (bottom panels) relations for SDSS (black dashed). With the DEM, the simulations produce dramatically different observables than when we do not include any dust prescription (Figure 2). Hence, dust must be account for when interpreting and comparing simulations. Moreover, with the DEMs, all three simulations produce observables consistent with SDSS. Since different simulations can produce reproduce observations by varying dust, dust significantly limits our ability to constrain the physical processes that go into galaxy simulations.

gas and metals. They find bluer red sequence peaks and a narrower blue cloud compared to SDSS. Although they compare the color distribution for all galaxies in M_* bins, we find neither of these discrepancies with the DEM.

Despite the success of the DEM, there are still some discrepancies with SDSS. For instance, the DEM produces broader distributions overall observations. Central galaxies in SDSS sharply cut-off above the red sequence while some galaxies in the DEM extend above this cut-off. The DEM color-magnitude relations also extend more broadly to higher luminosities than SDSS. For SIMBA, the DEM predicts a significant number of luminous ($M_r < -21$) blue galaxies not found in observations. Nonetheless, *with the DEM, we produce optical and UV color-magnitude relations that are in overall good agreement with observations, better than previous works, for three different hydrodynamical simulations: SIMBA, TNG, and EAGLE.*

Figure 5 also highlights the fact that any comparison of simulations must include dust attenuation. Dust dramatically changes the predicted observables of simulations. Without dust (Figure 2), we did not find a clearly bimodality in the optical color-magnitude relation and the simulations predicted UV colors outside of the range of observations. But with a simple framework for dust motivated by attenuation laws and correlation with galaxy properties, such as the DEM, simulations can reproduce observations.

These results highlight another key point. Robustly interpreting subgrid physics in simulations requires marginalizing over dust. Even for three simulations that produce significantly different SMFs and $M_* - \text{SFR}$ relations (Figure 1), the DEM is able to produce observables that agree with observations. In fact for SIMBA, the DEM reproduces the observations by assigning higher attenuation to star-forming galaxies so that they populate the red sequence while quiescent galaxies populate the blue cloud. This is due to the large number of low mass star-forming SIMBA galaxies that lie well above the SFS (Figure 1), which would otherwise all be luminous blue galaxies not found in observations. Our current understanding of dust, which is encapsulated in the DEM, has enough flexibility to reproduce observations for simulations that predict galaxy populations with different physical properties, even if it means contradicting the established relationship between color and SFR. Then marginalizing over dust would leave little constraining power on the subgrid galaxy physics of the simulations. Therefore, *current limitations in our understanding of dust in galaxies significantly impedes our ability to investigate galaxy formation from simulations.*

In addition to reproducing observations, DEM also provides insight into dust in galaxies. Given the parameterization of the DEM, it is especially easy to interpret correlation between dust attenuation and galaxy physical properties. In all three simulations, we find significant positive M_* dependence of τ_V , $m_{\tau, M_*} \sim 2$ (Figure 4), consistent with previous works in the literature. Burgarella et al. (2005), for instance, found significant positive M_* dependence in FUV attenuation in NUV-selected and FIR-selected samples. Garn & Best (2010) and Battisti et al. (2016) also find positive M_* dependence in SDSS star-forming galaxies. Most recently, Salim et al. (2018) find higher V and FUV attenuation for more massive star-forming galaxies in the GALEX-SDSS-WISE Legacy Catalog 2 (GSWLC2). With the DEM we confirm that *galaxies with higher M_* have overall higher dust attenuation.*

In addition to the M_* dependence, the DEM posteriors also reveal the correlation between dust attenuation and star formation. We focus only on TNG and EAGLE since SIMBA flips the color versus SFR relation. We infer DEM posteriors with $m_{\tau, \text{SFR}} \sim -1$ — galaxies with lower SFR have higher attenuation. While observations have examined the relationship between dust attenuation and SFR (*e.g.* Garn & Best 2010; Reddy et al. 2015; Battisti et al. 2016, 2017), they focus solely on star-forming galaxies. They find that star-forming galaxies with higher SFR have higher attenuation; however, this trend is driven by the M_* dependence since star-forming galaxies lie on the star-forming sequence (Garn & Best 2010; Battisti et al. 2017). At fixed M_* , observations find no strong SFR dependence for the star-forming population. Since previous works do not include quiescent galaxies, the DEM provides new insight into the SFR dependence of dust attenuation: *quiescent galaxies have overall higher dust attenuation.*

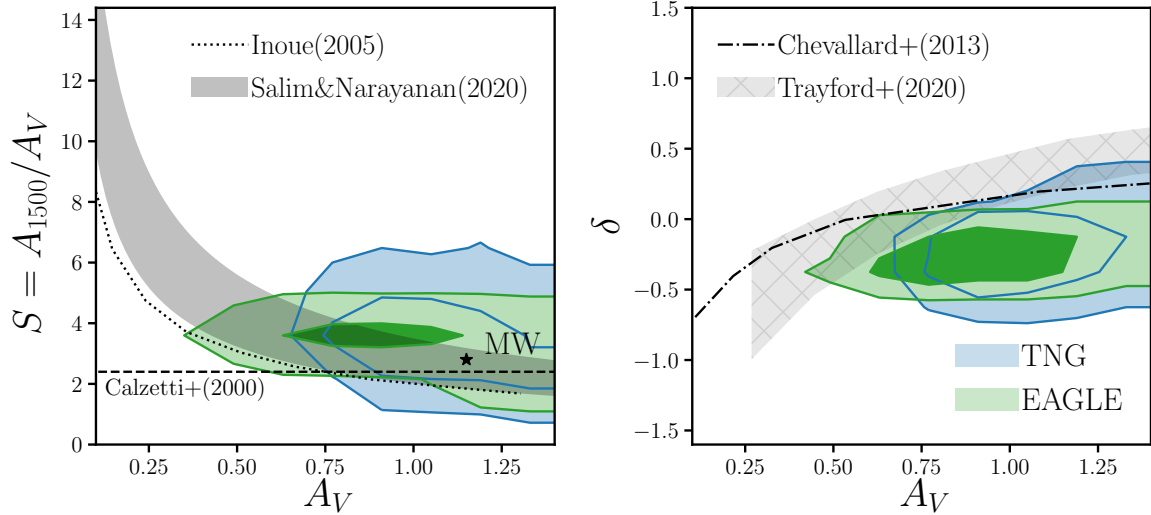


Figure 6. The attenuation-slope relation for TNG (blue) and EAGLE (green) simulations with the DEM. We present the relation using two different measurements of slope, commonly used in the literature: $S = A(1500\text{\AA})/A_V$ (left panel) and the slope offset from the Calzetti (2001) curve, δ (right panel). The DEM models predict an attenuation-slope relation, where the slope is steeper at lower attenuation, consistent with both observations and simulation. The DEM models only include massive galaxies, hence, they do not include many galaxies with low attenuation. At $A_V > 0.5$, however, the DEM models are in good agreement with observations Salim & Narayanan (2020). In fact, the DEM models match the observed attenuation-slope relation better than radiative transfer simulations, which predict attenuation curves that are too shallow (Inoue 2005; Chevallard et al. 2013; Trayford et al. 2020)

Our results also shed light on the slope of dust attenuation and its correlation to galaxy properties. In Figure 6, we present the attenuation-slope relation for TNG (blue) and EAGLE (green) with the DEM. The left and right panels present two different measurements of the slope $S = A(3000\text{\AA})/A_V$, which is easier to constrain in observations, and δ , the slope offset from the Calzetti (2001) curve that we use in the DEM. We include the attenuation and slope for the Milky Way (star) for reference. TNG and EAGLE both predict slopes within $2 < S < 5$ and centered around $S \sim 3.5$. In comparison, Leja et al. (2017) and Salim et al. (2018) find a broader range of slopes in their galaxy samples, $2 < S < 15$. However, this is because their sample includes galaxies with $A_V < 0.4$ that have steeper slopes. Excluding these galaxies, which are not in our sample, we find good agreement with Leja et al. (2017) and Salim et al. (2018). Other observations find slopes within the range $2 < S < 5$ for star-forming galaxies (Calzetti et al. 2000; Burgarella et al. 2005; Johnson et al. 2007; ?; Wild et al. 2011; Battisti et al. 2016, 2017). Therefore, *the dust attenuation curve slopes predicted by the DEM for TNG and SIMBA are in excellent overall agreement with observations.*

With the DEM, we can also examine the correlation between attenuation curve slopes and galaxy properties. For TNG and EAGLE, we find that the slope of the attenuation curve does not depend significantly on M_* or SFR. Leja et al. (2017) find composite and AGN galaxies generally have shallower slopes, although their sample is limited to only 129 galaxies. In contrast, Salim et al. (2018) find that quiescent galaxies in the GALEX-SDSS-WISE Legacy Catalog 2 (GSWLC2; Salim

& Boquien 2019) have significantly steeper curves. They, however, also find significantly steeper curves for the starburst population (*i.e.* galaxies above the SFS). With no consensus in the literature and few observations that examine the correlation between δ and galaxy properties, the lack of M_* and SFR dependence we find on δ is an interesting prediction for future observations.

Next, we examine the attenuation-slope relation. At low attenuation, dust scattering dominates absorption. In this regime, the attenuation curve steepens because red light tends to scatter isotropically while blue light tends to forward scatter, which causes more optical-to-IR light to escape the galaxy than UV light (Witt & Gordon 2000; ?). On the other hand, at high attenuation dust absorption is dominant and the attenuation curve is shallower (Chevallard et al. 2013). In both panels of Figure 6, the DEM predicts attenuation-slope relations where the slope is steeper at lower attenuation. Furthermore, for the A_V range probed by the DEM, the DEM A_V -slope relations are consistent with the $A_V - S$ relation of GSWLC2 galaxies (black shaded Salim & Narayanan 2020). They are also consistent with Leja et al. (2017). We also compare our results to theoretical predictions from radiative transfer models (Inoue 2005; Chevallard et al. 2013; Trayford et al. 2020). Inoue (2005) (dotted), the radiative transfer models considered in Chevallard et al. (2013) (dot dashed), and Trayford et al. (2020) (light shaded) all predict shallower attenuation curves than observations. This is also the case for the Narayanan et al. (2018) attenuation curves, not included in Figure 6. Therefore, the DEM not only predicts the established attenuation-slope relation, but it also better reproduces the observations than radiative transfer models.

Although the DEM does not explicitly model the complexities of dust-star geometry on a galaxy-by-galaxy basis, through the slab model and the dependence on galaxy properties, it includes significant variations in the dust attenuation. In Figure 7, we present the normalized attenuation curves of the TNG (blue) and EAGLE (green) DEM for low (top) and high M_* (bottom), star-forming (left) and quiescent galaxies (right). The attenuation curves are normalized at 3000\AA : $A(\lambda)/A(3000\text{\AA})$. The variation in the attenuation curves (1σ standard deviation about the median) is represented by the shaded region. For comparison, we include $A(\lambda)/A(3000\text{\AA})$ from observations (Calzetti et al. 2000; Battisti et al. 2017; Salim et al. 2018) as well as from simulations (Narayanan et al. 2018). The Calzetti et al. (2000) and Battisti et al. (2017) attenuation curves are for star-forming galaxies with significantly lower M_* . The Battisti et al. (2017) curve, for instance, is derived from $M_* < 10^{9.9} M_\odot$ star-forming galaxies. Meanwhile, the Salim et al. (2018) curves we include are specifically for $10^{9.5} < M_* < 10^{10.5} M_\odot$ star-forming galaxies (top left), $10^{10.5} < M_* M_\odot$ star-forming galaxies (bottom left), and quiescent galaxies (top and bottom right panels).

Focusing first on the attenuation curves of star-forming galaxies (left panels), we find that the Calzetti et al. (2000) and Battisti et al. (2017) curves are significantly shallower than the TNG and EAGLE DEM attenuation curves. Part of this discrepancy is driven by differences in M_* . Although we do not probe to low M_* , since the TNG and EAGLE attenuation curves get shallower at lower M_* , we expect better agreement with Calzetti et al. (2000) and Battisti et al. (2017) at the M_* ranges they probe. Next, compared to Salim et al. (2018), we find good agreement among the attenuation curves for star-forming galaxies. Furthermore, the variation in the DEM attenuation curves of star-forming galaxies is consistent with the variation in Figure 9 of Salim et al. (2018). The DEM attenuation

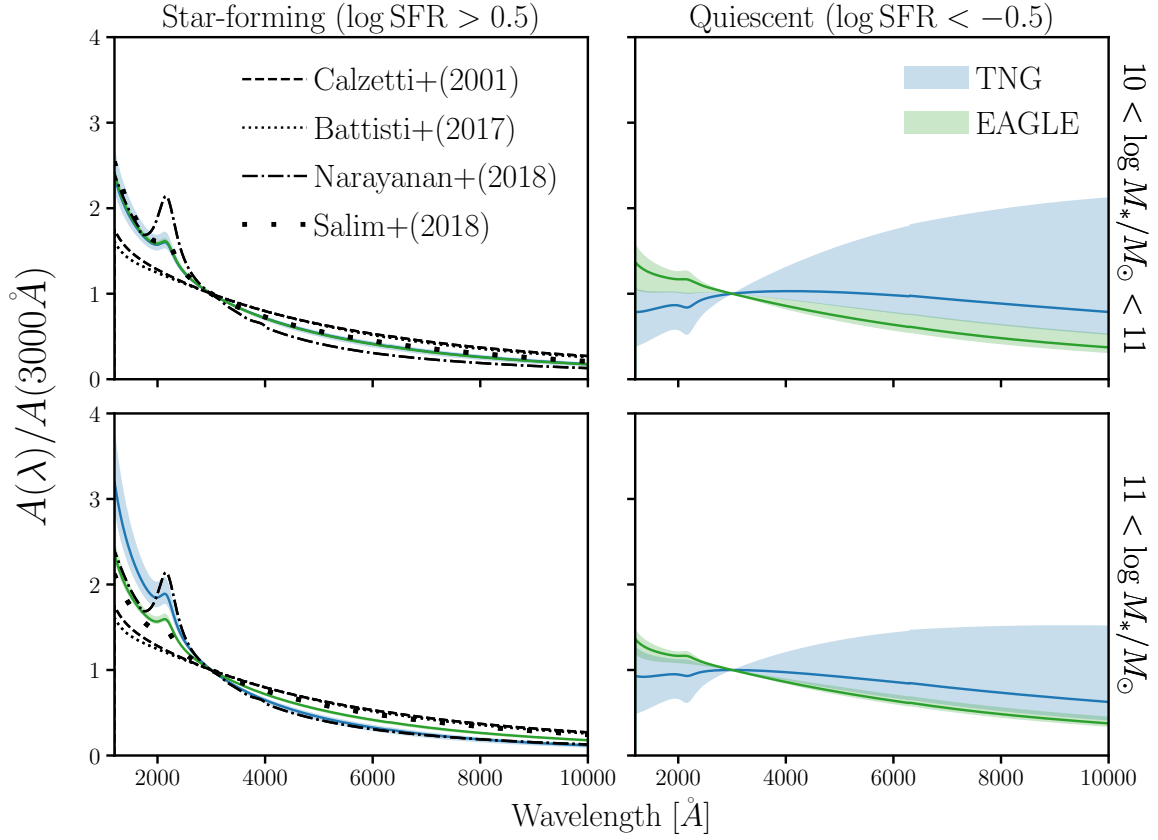


Figure 7. Attenuation curves of the TNG (blue) and EAGLE (green) DEM models for low (top) and high M_* (bottom), star-forming (left) and quiescent galaxies (right). The attenuation curves are normalized at 3000\AA : $A(\lambda)/A(3000\text{\AA})$. We mark the 1σ standard deviation of the attenuation curves with the shaded region. For comparison, we include measurements of $A(\lambda)/A(3000\text{\AA})$ from observations (Battisti et al. 2017; Salim et al. 2018) as well as from simulations (Narayanan et al. 2018). For star-forming galaxies, the Calzetti et al. (2000) and Battisti et al. (2017) attenuation curves are shallower than the DEM attenuation curves; however, this is primarily driven by the differences in M_* ranges. For Salim et al. (2018), which probe a similar M_* range as our DEM models, we find good agreement. We also find good agreement with median attenuation curve of Narayanan et al. (2018). With DEM models, we can also constrain the attenuation curves of quiescent galaxies, which are challenging to observationally constrain. Quiescent galaxies, have significantly shallower attenuation curves with larger variations in slope.

curves are also in excellent agreement with the median attenuation curve of Narayanan et al. (2018) star-forming galaxies. While Narayanan et al. (2018) find larger variations than the DEM, this is in part because of their broader M_* range. Hence, *for star-forming, the DEM find significant variation in dust attenuation consistent with both observations and simulations.*

In addition to constraining the attenuation curve of star-forming galaxies, the DEM models also shed light on dust attenuation in quiescent galaxies, which is particularly valuable due to the observational challenges of measuring dust attenuation in quiescent galaxies. For instance, MIR emission from active galactic nuclei (AGN) heating nearby dust complicates methods that rely on IR luminosity to measure dust attenuation Kirkpatrick et al. (2015). Even SED fitting methods require accounting

for AGN MIR emission (Salim et al. 2018) in addition to the overall challenge of breaking the degeneracy between SFH and metallicity to fit the continuum of quiescent galaxy SEDs (CH: cite?). With DEM models, which take a forward modeling approach with optical and UV data, we do not face these issues and can constrain the attenuation curves of quiescent galaxies. For both TNG and EAGLE, we find that quiescent galaxies have shallower attenuation curve with large variations in the slopes (Figure 7). We also find that they have higher $A_V \gtrsim 1.25$. CH: explanation for why DEM model does this In Leja et al. (2017), they similar find composite and AGN galaxies to have shallow attenuation curves with higher A_V ; however, the comparison is limited due to their smaller sample size (129 galaxies). In contrast, Salim et al. (2018) find that quiescent galaxies in GSWLC2 have significantly steeper curves; they, however, focus their analysis mainly on star-forming galaxies.

In our DEM model, we neglect the galaxies with $\text{SFR}=0$ from simulations by directly sampling the quiescent galaxy observables (Section A). Since galaxies with $\text{SFR}=0$ predicted by the simulations do not have recent star-formation and also have 0 gas mass@tjitske is this for all sims, we would expect them to also have no dust. However, a DEM model where we do not attenuate $\text{SFR}=0$ galaxies struggles to reproduce observations. This likely highlights the limitations of hydrodynamical simulations near the mass and temporal resolutions as well as the limitations of subgrid prescriptions for gas. CH: Uncertainties in the dust destruction timescale may also contribute to the explanation (e.g. Jones & Nuth 2011; Slavin et al. 2015). We emphasize that our prescription for $\text{SFR}=0$ galaxies ensures that they do not significantly impact the constraints on DEM parameters.

TODO

For the DEM model in this paper, we fix the amplitude of the UV dust bump to the amplitude of δ (Eq. ??). If, rather than fixing m_E and c_E in Eq. ??, we allow them to be free parameters we find little constraining power on these parameters. More importantly, we find consistent constraints for the other DEM parameters, which implies that fixing the UV bump parameters does not impact our results.

A major assumption in the DEM model is how we sample the A_V using the slab model. For each simulated galaxy, the DEM model uniformly samples the inclination and then assigns A_V with the slab model (Eq. 3). As we detail in Section 3, this slab model is consistent inclination dependence of attenuation found in both observations (e.g. Salim & Narayanan 2020) and simulations (Chevallard et al. 2013; Narayanan et al. 2018; Trayford et al. 2020, e.g.). Moreover, the slab model successfully reproduces the A_V distribution of SDSS galaxies (Figure 8). To ensure that our results do not hinge on the slab model, we conduct our analysis using a truncated normal distribution based DEM model to sample A_V (Appendix B). This model is more flexible than the slab model. For instance, we include physical parameter dependence for the scatter of A_V , and not just for τ_V . We refer readers to Appendix B for details. We find that adding our results are not impacted by the change in the A_V sampling model or the added flexibility. Therefore, our results are not driven by our choice of the slab model.

CH: How about our prior choice?

CH: what we learn about in the simulations

CH: what we learn about dust paragraph on restating how we can learn about dust through DEMs based on trends we see across all simulations. summarize main findings again.

CH: observables unaffected by dust/dem? Are there observables that hydro sims + DEMs cannot reproduce? What does that say about the hydro sims? What observables are unaffected by DEMs? We should chase those observables.

CH: don't over-interpret observations We clearly have to be careful with overinterpreting hydro sims because modifying dust allows us to reproduce whatever we want.

- Should we bother calibrating our empirical and semi-analytic models to hydrodynamic simulations when the hydro sims also require marginalizing over dust parameters? Does this mean that if our goal is to make realistic mocks, we can be relatively careless about

CH: What are some applications for DEMs? Realistic mock catalogs that reproduce observations in observable-space rather than physical parameter space. **CH: talk about IQ paper where we use best-fit dust**

6. SUMMARY

ACKNOWLEDGEMENTS

It's a pleasure to thank ... This material is based upon work supported by the U.S. Department of Energy, Office of Science, Office of High Energy Physics, under contract No. DE-AC02-05CH11231. This project used resources of the National Energy Research Scientific Computing Center, a DOE Office of Science User Facility supported by the Office of Science of the U.S. Department of Energy under Contract No. DE-AC02-05CH11231.

APPENDIX

A. RESOLUTION EFFECTS

Figure demonstrating imprint SFR=0 leave on the observable space and how we deal with them so we can ignore them...

B. BEYOND THE SLAB DEM

A major assumption of our fiducial DEM is that we sample the amplitude of attenuation from the slab model. The slab model makes the simplifying assumption that dust in galaxies are in a slab-like geometry and illuminated by the stellar radiation source (Somerville & Primack 1999). Then, for a given τ_V , the attenuation depends solely on the orientation of the galaxy. This simplification, ignores any complexities in the star-to-dust geometry that impact the shape of the attenuation curve (Witt Gordon 1996, 2000, Seon Drain 2016).

Besides its simplifications, the slab model predicts A_V distribution with significant differences than the A_V distributions measured from observations. In Figure 8, we compare the A_V distribution predicted by the slab model (black) to the A_V distribution of star-forming galaxies in our SDSS sample (blue). The A_V values are derived using SED fitting from the Brinchmann et al. (2004) MPA-JHU catalog and how are the SF galaxies classified. The slab model A_V values are derived using Eq. 3 and 4 with M_* s and SFRs from the same SDSS sample and the inclinations, i , are uniformly sampled over the range $[0, \pi/2]$. With $\{m_{\tau,1}, m_{\tau,2}, c_{\tau}\}$ chosen to reproduce the observed A_V distribution, the

TODO

TODO

slab model can reproduce the overall shape. However, it predicts an extended high A_V tail not found in observations.

Given these shortcomings of the slab model, we want to ensure that our results do not hinge on the slab model. Modeling the star-to-dust geometries with increased complexities, however, would involve expensive hydrodynamic simulations and dust radiative transfer calculations (*e.g.* Narayanan et al. 2018)jonsson2006, rocha2008, natale2015,hayward smith2015,hou2017,trayford2020. We instead take an empirical approach and implement a flexible model for sampling A_V based on a truncated normal distribution: TODO

$$A_V \sim \mathcal{N}_T(\mu_{A_V}, \sigma_{A_V}) = \frac{\mathcal{N}(\mu_{A_V}, \sigma_{A_V})}{1 - \Phi\left(-\frac{\mu_{A_V}}{\sigma_{A_V}}\right)}. \quad (\text{B1})$$

Here, \mathcal{N} is the standard normal distribution and $\Phi(x) = \frac{1}{2} (1 + \text{erf}(x/\sqrt{2}))$ is the cumulative distribution function of \mathcal{N} . μ_{A_V} and σ_{A_V} are the mean and variance of the truncated normal distribution. Similar to Eq. 4, we allow μ_{A_V} and σ_{A_V} to depend on the physical properties of galaxies:

$$\mu_{A_V} = m_{\mu,1}(\log M_* - 10.) + m_{\mu,2} \log \text{SFR} + c_{\mu} \quad (\text{B2})$$

$$\sigma_{A_V} = m_{\sigma,1}(\log M_* - 10.) + m_{\sigma,2} \log \text{SFR} + c_{\sigma}. \quad (\text{B3})$$

The A_V distribution from our truncated normal (orange dashed) closely reproduces the observed SDSS A_V distribution (Figure 5). N_T is able to reproduce the overall skewness but unlike the slab model, it does not have a long high A_V tail. With more free parameters and a functional form that closely resembles the observed A_V distribution, the truncated normal model provides a flexible alternative to the slab model and we include it in our analysis.

REFERENCES

- Abazajian K. N., et al., 2009, [The Astrophysical Journal Supplement Series](#), 182, 543
- Alsing J., Wandelt B., Feeney S., 2018, [arXiv:1801.01497 \[astro-ph\]](#)
- Anglés-Alcázar D., Davé R., Faucher-Giguère C.-A., Özel F., Hopkins P. F., 2017, [Monthly Notices of the Royal Astronomical Society](#), 464, 2840
- Baes M., Trčka A., Camps P., Nersesian A., Trayford J., Theuns T., Dobbels W., 2019, [arXiv:1901.08878 \[astro-ph\]](#)
- Battisti A. J., Calzetti D., Chary R.-R., 2016, [The Astrophysical Journal](#), 818, 13
- Battisti A. J., Calzetti D., Chary R.-R., 2017, [The Astrophysical Journal](#), 840, 109
- Beaumont M. A., Cornuet J.-M., Marin J.-M., Robert C. P., 2009, [Biometrika](#), 96, 983
- Blanton M. R., Roweis S., 2007, [The Astronomical Journal](#), 133, 734
- Blanton M. R., et al., 2005, [The Astronomical Journal](#), 129, 2562
- Booth C. M., Schaye J., 2009, [Monthly Notices of the Royal Astronomical Society](#), 398, 53
- Brinchmann J., Charlot S., White S. D. M., Tremonti C., Kauffmann G., Heckman T., Brinkmann J., 2004, [Monthly Notices of the Royal Astronomical Society](#), 351, 1151
- Burgarella D., Buat V., Iglesias-Páramo J., 2005, [Monthly Notices of the Royal Astronomical Society](#), 360, 1413
- Calzetti D., 2001, [New Astronomy Reviews](#), 45, 601
- Calzetti D., Armus L., Bohlin R. C., Kinney A. L., Koornneef J., Storchi-Bergmann T., 2000, [The Astrophysical Journal](#), 533, 682
- Cameron E., Pettitt A. N., 2012, [Monthly Notices of the Royal Astronomical Society](#), 425, 44

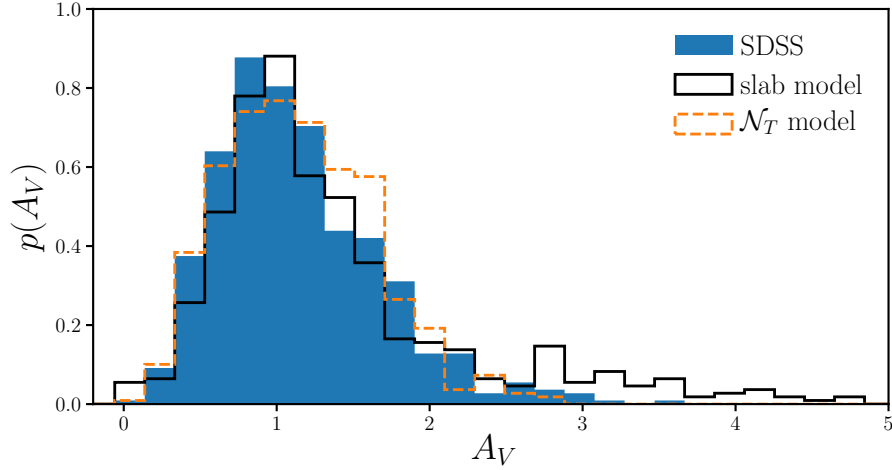


Figure 8. Comparison of A_V distribution of SDSS star-forming galaxies (blue) to predictions from the slab model (Eq. 3; black). **detail on how SDSS SF galaxies are classified.** The slab model assumes that there’s a slab of dust in front of a galaxy. We use $\tau_V = 2$ for the slab model above. Regardless of τ_V , however, the slab model predicts a significantly more asymmetric and peaked A_V distribution than observations. Given this disagreement, *we include in our analysis a DEM with an empirical prescription for A_V based on a truncated normal distribution, which better reproduce the observed A_V distribution* (Section B).

Camps P., Baes M., 2015, [Astronomy and Computing](#), 9, 20

Chabrier G., 2003, [Publications of the Astronomical Society of the Pacific](#), 115, 763

Chevallard J., Charlot S., Wandelt B., Wild V., 2013, [Monthly Notices of the Royal Astronomical Society](#), 432, 2061

Crain R. A., et al., 2015, [Monthly Notices of the Royal Astronomical Society](#), 450, 1937

Dalla Vecchia C., Schaye J., 2012, [Monthly Notices of the Royal Astronomical Society](#), 426, 140

Davé R., Thompson R., Hopkins P. F., 2016, [Monthly Notices of the Royal Astronomical Society](#), 462, 3265

Davé R., Rafieferantsoa M. H., Thompson R. J., 2017a, [arXiv:1704.01135 \[astro-ph\]](#)

Davé R., Rafieferantsoa M. H., Thompson R. J., Hopkins P. F., 2017b, [Monthly Notices of the Royal Astronomical Society](#), 467, 115

Davé R., Anglés-Alcázar D., Narayanan D., Li Q., Rafieferantsoa M. H., Appleby S., 2019, [Monthly Notices of the Royal Astronomical Society](#), 486, 2827

Del Moral P., Doucet A., Jasra A., 2012, [Statistics and Computing](#), 22, 1009

Diggle P. J., Gratton R. J., 1984, [Journal of the Royal Statistical Society. Series B \(Methodological\)](#), 46, 193

Garn T., Best P. N., 2010, [Monthly Notices of the Royal Astronomical Society](#), 409, 421

Genel S., et al., 2014, [Monthly Notices of the Royal Astronomical Society](#), 445, 175

Hahn C., Vakili M., Walsh K., Hearin A. P., Hogg D. W., Campbell D., 2017a, [Monthly Notices of the Royal Astronomical Society](#), 469, 2791

Hahn C., Tinker J. L., Wetzel A. R., 2017b, [The Astrophysical Journal](#), 841, 6

Hahn C., Tinker J. L., Wetzel A., 2019a, [arXiv:1910.01644 \[astro-ph\]](#)

Hahn C., Beutler F., Sinha M., Berlind A., Ho S., Hogg D. W., 2019b, [Monthly Notices of the Royal Astronomical Society](#), 485, 2956

Hahn C., et al., 2019c, [The Astrophysical Journal](#), 872, 160

Handley W., Millea M., 2019, [Entropy](#), 21, 272

Hopkins P. F., 2015, [Monthly Notices of the Royal Astronomical Society](#), 450, 53

Hopkins P. F., et al., 2017, [arXiv:1707.07010 \[astro-ph\]](#)

Inoue A. K., 2005, [Monthly Notices of the Royal Astronomical Society](#), 359, 171

- Ishida E. E. O., et al., 2015, [Astronomy and Computing](#), 13, 1
- Johnson B. D., et al., 2007, [The Astrophysical Journal Supplement Series](#), 173, 392
- Jones A. P., Nuth J. A., 2011, [Astronomy and Astrophysics](#), 530, A44
- Kirkpatrick A., Pope A., Sajina A., Roebuck E., Yan L., Armus L., Díaz-Santos T., Stierwalt S., 2015, [The Astrophysical Journal](#), 814, 9
- Kriek M., Conroy C., 2013, [The Astrophysical Journal Letters](#), 775, L16
- Leja J., Johnson B. D., Conroy C., van Dokkum P. G., Byler N., 2017, [The Astrophysical Journal](#), 837, 170
- Lin C.-A., Kilbinger M., Pires S., 2016, [Astronomy and Astrophysics](#), 593, A88
- McAlpine S., et al., 2016, [Astronomy and Computing](#), 15, 72
- Narayanan D., Conroy C., Davé R., Johnson B. D., Popping G., 2018, [The Astrophysical Journal](#), 869, 70
- Nelson D., et al., 2015, [Astronomy and Computing](#), 13, 12
- Nelson D., et al., 2018, [Monthly Notices of the Royal Astronomical Society](#), 475, 624
- Noll S., Burgarella D., Giovannoli E., Buat V., Marillac D., Muñoz-Mateos J. C., 2009, [Astronomy and Astrophysics](#), 507, 1793
- Pillepich A., et al., 2018, [Monthly Notices of the Royal Astronomical Society](#), 473, 4077
- Pritchard J. K., Seielstad M. T., Perez-Lezaun A., Feldman M. W., 1999, [Molecular Biology and Evolution](#), 16, 1791
- Reddy N. A., et al., 2015, [The Astrophysical Journal](#), 806, 259
- Salim S., Boquien M., 2019, [The Astrophysical Journal](#), 872, 23
- Salim S., Narayanan D., 2020, [arXiv:2001.03181 \[astro-ph\]](#)
- Salim S., Boquien M., Lee J. C., 2018, [The Astrophysical Journal](#), 859, 11
- Schaye J., et al., 2015, [Monthly Notices of the Royal Astronomical Society](#), 446, 521
- Slavin J. D., Dwek E., Jones A. P., 2015, [The Astrophysical Journal](#), 803, 7
- Somerville R. S., Primack J. R., 1999, [Monthly Notices of the Royal Astronomical Society](#), 310, 1087
- Somerville R. S., Gilmore R. C., Primack J. R., Domínguez A., 2012, [Monthly Notices of the Royal Astronomical Society](#), 423, 1992
- Springel V., 2005, [Monthly Notices of the Royal Astronomical Society](#), 364, 1105
- Springel V., et al., 2018, [Monthly Notices of the Royal Astronomical Society](#), 475, 676
- Tavare S., Balding D. J., Griffiths R. C., Donnelly P., 1997, [Genetics](#), 145, 505
- Tinker J., Wetzel A., Conroy C., 2011, preprint, 1107, [arXiv:1107.5046](#)
- Tinker J. L., Hahn C., Mao Y.-Y., Wetzel A. R., Conroy C., 2018, [Monthly Notices of the Royal Astronomical Society](#), 477, 935
- Trayford J. W., et al., 2015, [Monthly Notices of the Royal Astronomical Society](#), 452, 2879
- Trayford J. W., et al., 2017, [Monthly Notices of the Royal Astronomical Society](#), 470, 771
- Trayford J. W., Lagos C. d. P., Robotham A. S. G., Obreschkow D., 2020, [Monthly Notices of the Royal Astronomical Society](#), 491, 3937
- Tress M., et al., 2018, [Monthly Notices of the Royal Astronomical Society](#), 475, 2363
- Vogelsberger M., et al., 2014, [Monthly Notices of the Royal Astronomical Society](#), 444, 1518
- Weinberger R., et al., 2018, [Monthly Notices of the Royal Astronomical Society](#), 479, 4056
- Weyant A., Schafer C., Wood-Vasey W. M., 2013, [The Astrophysical Journal](#), 764, 116
- Wild V., Charlot S., Brinchmann J., Heckman T., Vince O., Pacifici C., Chevallard J., 2011, [Monthly Notices of the Royal Astronomical Society](#), 417, 1760
- Witt A. N., Gordon K. D., 2000, [The Astrophysical Journal](#), 528, 799